Proton imaging detection of transient electromagnetic fields in laser-plasma interactions (invited)

M. Borghesi[a)]
Department of Pure and Applied Physics, The Queen's University of Belfast, Belfast, United Kingdom

A. Schiavi, D. H. Campbell, and M. G. Haines
The Blackett Laboratory, Imperial College of Science, Technology and Medicine, London, United Kingdom

O. Willi
Institut für Laser- und Plasmaphysik, Heinrich-Heine-Universität, Düsseldorf, Germany

A. J. Mackinnon and P. Patel
Lawrence Livermore National Laboratory, Livermore, California

M. Galimberti and L. A. Gizzi
Istituto per i Processi Chimico-Fisici, CNR, Pisa, Italy

(Presented on 9 July 2002)

Due to their particular properties (small source size, low divergence, short duration, large number density), the beams of multi-MeV protons generated during the interaction of ultraintense ($I > 10^{19}$ W/cm^2) short pulses with thin solid targets are most suited for use as a particle probe in laser–plasma experiments. In particular, the proton beams are a valuable diagnostic tool for the detection of electromagnetic fields. The recently developed *proton imaging* technique employs the beams, in a point-projection imaging scheme, as an easily synchronizable diagnostic tool in laser–plasma interactions, fields, with high temporal and spatial resolution. The broad energy spectrum of the beams coupled with an appropriate choice of detector (multiple layers of dosimetric film) allows temporal multiframe capability. By allowing, for the first time, diagnostic access to electric-field distributions in dense plasmas, this novel diagnostic opens up to investigation a whole new range of unexplored phenomena. Results obtained in experiments performed at the Rutherford Appleton Laboratory are discussed here. In particular, the article presents the measurement of highly transient electric fields related to the generation and dynamics of hot electron currents following ultraintense laser irradiation of targets. The experimental capabilities of the technique and the analysis procedure required are well exemplified by the data presented.
[DOI: 10.1063/1.1534390]

I. INTRODUCTION

Self-generated electric and magnetic fields play a role of fundamental importance in many laser–plasma processes. This is particularly true in interactions employing short ultraintense laser pulses,[1,2] where enormous currents of very energetic electrons (up to 100–1000 MA) are instantaneously driven via several laser–electron coupling processes.[3–6] Ultralarge, quasistatic magnetic and electric fields can be generated either by the current flow or via the induced space-charge separation. Magnetic fields as large as 10^4–10^5 T (Ref. 7) and electric fields as large as 10^{12} V/m (Refs. 8 and 9) can be reached in solid target interactions with the laser intensities presently available (up to 10^{20} W/cm^2). The transport of these enormous currents, a critical issue for applications such as the fast ignitor scheme for inertial confinement fusion,[10] is also greatly affected by self-generated electric and magnetic fields, both on macroscopic[8,11,12] and microscopic[13,14] spatial scales.

Diagnostics able to provide meaningful and direct measurements of quasistatic electromagnetic fields under intense irradiation conditions are, therefore, of extreme importance as they can significantly advance the understanding of these fundamental issues. Self-generated quasistatic magnetic fields in laser–produced plasmas have been usually revealed via the Faraday rotation effect.[15] However, this technique can be used efficiently only with plasmas of relatively low electron density (well below the critical density for the wavelength of an optical probe). Recently, a novel method has been applied to the measurement of ultralarge magnetic fields in laser–solid interaction experiments.[16] The magnitude of the fields is deduced from the observation of the properties of the harmonics of the fundamental laser wavelength emitted during the interaction.

Techniques for direct electric-field detection in high-temperature laser-produced plasmas are much less developed. The use of charged particle beams for electric-field detection in plasmas via the associated deflection seems an obvious choice, and indeed it has been used in the past, although rarely. Mendel and Olsen used beams of 22 keV He+ ions for the detection of small charge-separation electric fields in the low-density blow-off plasma produced on a

a)Electronic mail: m.borghesi@qub.ac.uk

laser irradiated target.[17] A similar technique, employing 100 keV protons, has been successively used for the investigation of collective ion acceleration by relativistic electron beams.[18] In practice, the difficulties and high cost involved in coupling externally produced particle beams of sufficiently high energy to laser–plasma experiments (or indeed magnetic confinement experiments) has limited the application of such diagnostic techniques. A further limitation has been the length of the ion pulses provided by conventional accelerators (typically in the ns regime), which would make impossible the detection of the transient electric fields associated with laser–plasma high-intensity interactions.

Fortunately, the ideal tool for electromagnetic field detection in dense plasmas is provided by the high-intensity interactions themselves. Indeed, one of the most exciting results recently obtained in laser–plasma interaction experiments is the observation of very energetic beams of protons, generated during the interaction of ultraintense short pulses with solid targets. In a number of experiments, performed with different laser systems and in different interaction conditions, protons with energies up to several tens of MeV have been detected behind thin foils irradiated with high-intensity pulses.[19] The beams are directed along the normal to the back surface of the target, and are remarkably collimated at the highest energies. They have high brightness, short duration, and small apparent source size. These characteristics distinguish these beams from the less directed lower energy protons observed in earlier work at lower intensities,[20] and make them of exceptional interest as a particle probe.

Proton beams are observed even from targets which nominally do not contain hydrogen. In this case, they originate from hydrocarbon impurities located on the target surfaces.[20] Proposed theoretical models indicate that the protons gain most of their energy from the ultrahigh electric field ($\sim$MeV/μm) present during the interaction at the rear of the target.[21,22] These fields are set up by the space charge caused by laser-accelerated fast electrons escaping from the target.

In this article, the use of these proton beams as a particle probe for detection of electromagnetic fields in high-density matter investigations is presented.[23] The experimental tests were carried out at the Rutherford Appleton Laboratory, Chilton (UK), employing the Vulcan laser in the chirped pulse amplification (CPA) mode. The application of this technique has led to the first direct demonstration of highly transient electric fields following ultraintense laser–pulse interaction with plasmas and solids.

II. LASER AND PROTON BEAM PARAMETERS

Although some general characteristics are common to all experimental observations, the detailed properties of the beams depend on the parameters of the laser used to produce them and the characteristics of the targets employed. In the following, we will refer to the parameters of the proton beams obtained in the Vulcan laser experiments. This laser,[24] operating in the CPA mode provides 1.054 μm and 1 ps pulses with energy up to 100 J.

In the measurements reported in this article, however, due to setup restrictions, the energy available for proton production was about 25 J. When focused by an F/3.5 off-axis parabola, the focal spot varied between 8 and 10 μm in diameter at full width at half maximum (FWHM), containing 30%–40% of the energy, and giving intensities up to 10^{19} W/cm^2. The targets used for proton beam production were Al foils, 1–2 mm wide and 3 μm thick. The laser pulse was focused onto the center of the main target, at an angle of incidence of 15° with the target normal.

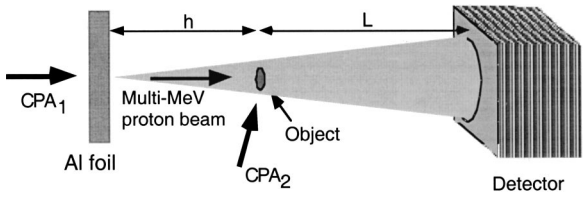

FIG. 1. Experimental arrangement for proton imaging. A CPA pulse (CPA_1) is used for producing a beam of protons which crosses the sample before reaching the detector. The other CPA pulse (CPA_2) drawn was used to interact with the sample and generate transient electromagnetic fields.

The proton beams produced under these conditions were bright typically containing about 10^{12} protons with energy above 3 MeV per shot. The protons were emitted from the rear of the target with small angular divergence (10°–15° half aperture), cutoff energy of about 10 MeV and temperature of $\sim$1.5 MeV (obtained by fitting a Boltzmann exponential to the proton spectrum).

An important property of the beam, observed with both laser systems, is that the protons appear to be emitted from a source with very limited spatial extent (less than 10 μm diameter). More details on this will be given in Sec. III.

III. PROTON IMAGING SETUP

Due to the small source size, one can use the beam to back illuminate a sample, in a point-projection imaging scheme, as shown in Fig. 1. The magnification of the system is determined by $M=1+L/h$, with L and h, respectively, as the object-to-detector and source-to-object distances. There is a one-to-one correspondence between the points of the object plane and the points on the detector plane. In general, the intensity distribution cross section of the proton beam is modified both by collisional stopping/scattering, and by deflections due to electric and magnetic fields. If the samples probed are thin enough and electromagnetic fields are present in and around the target, collisional effects become negligible and the diagnostic is mainly sensible to the fields. They deflect the protons, modifying the beam cross section at the detector plane and the one-to-one perfect imaging correspondence. From these modifications, the field distribution in and around the targets can be reconstructed, as will be seen in the following sections.

The detector employed consisted of several radiochromic films (RCF)[25] arranged in a stack. Each stack was protected by a 25 μm Al filter. In each RCF, two 15 μm layers of organic dye, separated by about 140 μm, are embedded in 270 μm thick plastic. The dye reacts to ionizing radiation. The two active layers can be separated mechanically after exposure. The equivalent dose of energetic protons stopped

in each layer can be measured from the changes in optical density undergone by the film, yielding information on the number and energy of the protons. Since protons deposit energy mainly in the Bragg peak at the end of their range and the number of the protons decreases with their energy, the signal on each active layer is mainly due to protons having energies within a narrow range. At any given distance from the proton beam axis, about 50% of the signal in an active layer is due to protons within an energy range δE_p of the order of 0.5 MeV. This estimate was obtained assuming a Boltzmann-type distribution with Te$\sim$1.5 MeV, and using Monte Carlo simulations of the proton propagation in the detector.[26]

The spatial resolution of the imaging arrangement is determined by two factors, the size d of the proton source and the width δs of the point spread function of the detector (mainly due to scattering near the end of the proton range). The latter can be determined, via Monte Carlo simulations, to be $\delta s \sim 20$ μm for a proton energy $E_p \sim 7$ MeV. The spatial resolution is, therefore, of the order of $\Delta s \sim \max(d, \delta s/M)$ where M is the magnification of the optical system. In the setup typically used, it was $M > 10$ and Δs was better than 10 μm.

The high spatial resolution of the diagnostic has been confirmed by several tests using static targets, which indicate an apparent source size of a few microns. The word ''apparent'' is used because there is experimental evidence that the protons are, in reality, emitted in a laminar fashion by a much larger area (with radius of the order of 100 μm).[27]

When probing transient phenomena, the temporal resolution of the diagnostic is of fundamental importance. The ultimate limit of the temporal resolution is given by the duration of the proton burst τ at the source. According to the models,[22,23] τ is of the order of the laser pulse duration ($\sim$1 ps). However, in the conditions of the field measurements reported in the following sections, other effects are more important. In particular, the finite energy resolution of the active layers and the finite transit time of the protons through the region where the fields are present limit the resolution to several ps (e.g., 4–5 ps for the layer corresponding to $E_p = 7$ MeV).

Energy dispersion provides the technique with an intrinsic multiframe capability. In fact, since the sample to be probed is situated at a finite distance from the source, protons with different energies reach it at different times. As the detector performs spectral selection, each RCF layer contains, in first approximation, information pertaining to a particular temporal delay.

The order of magnitude of the minimum electric field δE detectable is related to the spatial resolution Δs via the relation $\delta E \sim 2E_p M \Delta s / zL$, where z is the region over which the field extends, L is the source-to-detector distance, M is the magnification of the system, and E_p is expressed in eV. For our setup, taking for example $z \sim 200$ μm, one obtains $\delta E \sim 5 \times 10^8$ V/m.

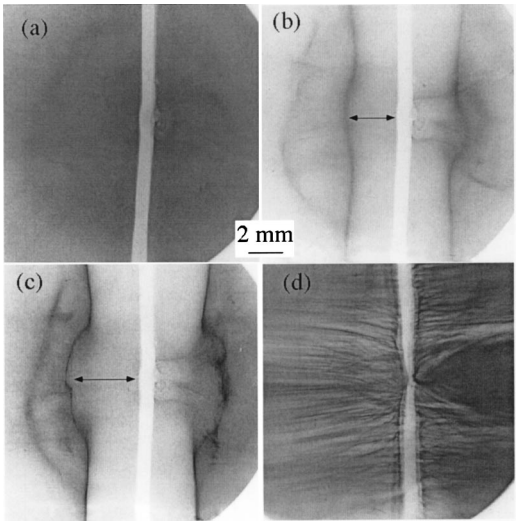

FIG. 2. Proton images taken following CPA irradiation of a 50 μm Ta wire. Each picture refers to different probing delay Δt from the interaction. The first three pictures are three active layers from the same shot: (a) $E_p \sim 8$ MeV, $\Delta t \sim -12$ ps, (b) $E_p \sim 7$ MeV, $\Delta t \sim -8$ ps, and (c) $E_p \sim 6$ MeV, $\Delta t \sim -3$ ps. The fourth image is taken from another shot in which the two CPA pulses were suitably delayed: (d) $E_p = 7$ MeV, $\Delta t = +30$ ps.

IV. MEASUREMENT OF HIGHLY TRANSIENT ELECTRIC CHARGING

This technique has unique capabilities for the detection of the onset and decay of highly transient electromagnetic fields. The data shown in the following provides an example of the novel phenomena, which can be investigated using the proton imaging technique. It also illustrates several of the diagnostic features just discussed.

Two 1 μm and 1 ps pulses (CPA_1 and CPA_2) produced by the Vulcan laser were focused onto separate targets at an intensity of 10^{19} W/cm^2. The CPA_2 pulse was focused onto an Al foil to produce a beam of protons, while the CPA_1 pulse was focused onto a separate sample. The delay between the two pulses could be varied optically. The angle between proton beam direction and CPA_1 propagation directions was approximately 75°. The distances involved were: $h = 2$ mm (Al foil to main target), and $L = 2.7$ cm (main target to detector), giving a magnification $M = 13.5$.

In Fig. 2, proton images taken (in a single shot) after ultraintense irradiation of a 50 μm Ta wire are shown. The layers displayed illustrate the multiframe capability of the diagnostic. Figures 2(a)–2(c) are three RCF layers from the same shot and refer to different probing times ahead of the peak of the interaction pulse: (a) $E_p \sim 8$ MeV, $\Delta t \sim -12$ ps, (b) $E_p \sim 7$ MeV, $\Delta t \sim -8$ ps, (c) $E_p \sim 6$ MeV, $\Delta t \sim -3$ ps; the fourth image is taken from another shot in which the two CPA pulses were suitably delayed, and (d) $E_p = 7$ MeV, $\Delta t = +30$ ps. In the earliest frame, the proton beam intensity cross section is undisturbed, apart from the collisional shadow of the target and some perturbations visible around the interaction area, due to the plasma created by the prepulse. In Figs. 2(b) and 2(c) corresponding to proton transit through the target close to the peak of the interaction pulse, the proton beam cross section is modified dramatically. Following the expulsion of hot electrons during the

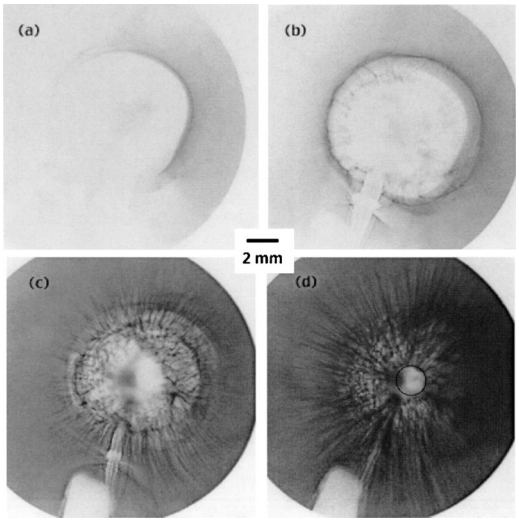

FIG. 3. Proton images taken following CPA irradiation of a 150 μm glass microballoon. The original size and position of the target are indicated by the black circle in (d). Each picture refers to different active layers (i.e., different proton energy E_p and different probing delay Δt from the interaction): (a) $E_p \sim 8$ MeV, $\Delta t \sim -2$, (b) $E_p \sim 7$ MeV, $\Delta t \sim 1.5$ ps, (c) $E_p \sim 4.5$ MeV, $\Delta t \sim 15$ ps, and (d) $E_p \sim 3$ MeV, $\Delta t \sim 30$ ps.

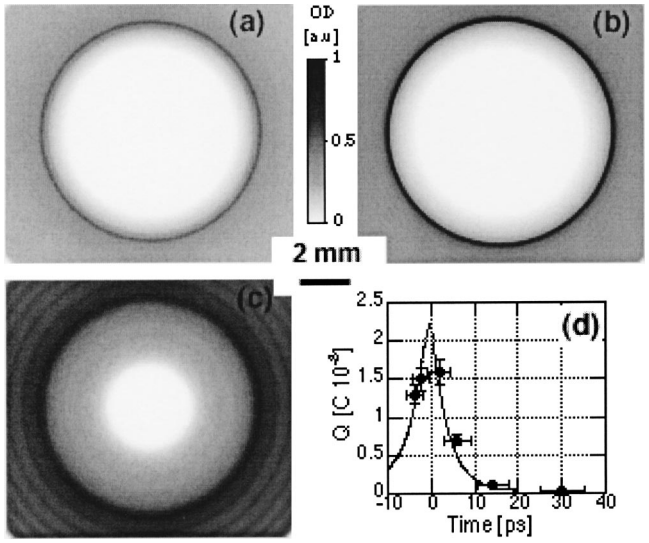

FIG. 4. (a)–(c): Particle tracing simulation results. The frames show the optical density distribution expected in the corresponding layers shown in Fig. 3 after propagation of the proton beam through the potential of a discharging microballoon. Distances and dimensions are as in the experiment. (d) Plot of target charge vs time. The points represent the electrostatic estimates obtained from the experimental layers. The continuous line is the temporal evolution of the charge used in the simulation. The rising part of the curve is a Lorentzian, followed by an exponential decay. The free parameters of the curve have been varied to optimize the match to the overall features of the experimental data.

interaction, the wire charges up positively and deflects the protons away from its surface. The charge up starts between 5 and 10 ps ahead of the peak of the pulse. In fact, although the FWHM of the laser pulse is 1 ps, it takes several ps for the intensity to rise from the pedestal level to the peak. At the time of (c) the intensity on target is already high enough to start to produce efficiently energetic electrons (few hundreds of keV). A difference in the beam cross section patterns in Figs. 2(b) and 2(c) is clearly visible, meaning that the electric-field distribution around the wires has changed in a 5 ps time interval. Ahead of the peak of the interaction pulse, the wire charges up positively and deflects the protons. The charge up begins 5–10 ps before the peak of the pulse, when the intensity on target due to the rising edge of the pulse[13] will be in the 10^{16}–10^{17} W/cm^2 range. The target remains charged, deflecting the protons, for a few tens of picosecond.

By matching the observed proton deflection to two-dimensional particle-tracing results, the temporal evolution of target charge and electric field can be inferred. The field at the target surface (at the position indicated by the arrow in Fig. 2) varies between 1.5×10^{10} V/m in Fig. 2(b) and 2.0×10^{10} V/m in Fig. 2(c). After 30 ps, no deflection is observed meaning that the maximum field is less than $\sim 5\times10^{8}$ V/m.

Figure 3 shows proton images taken, again in a single shot, after ultraintense irradiation of a 150 μm diam glass microballoon. Even in this case, the protons are deflected away from the target by an outwardly directed electric field. The experimental deflection can be matched to the predicted deflection for protons propagating in the Coulomb field of a static charge. By using this method, the charge of the target and, consequently, the electric field near the surface can be estimated at various times. By taking, for example, the layer of Fig. 3(c), the deflection is consistent with $Q \sim 1.5\times10^{-8}$ C, giving again a field of about 10^{10} V/m near the target surface.

However, associating a time to each layer is only valid in first approximation. In order to interpret more fully the data of Fig. 3, three-dimensional particle-tracing simulations of proton propagation in the field of a discharging sphere were performed. Simulation results for the various layers are shown in Fig. 4. The particle tracing routine is helpful in identifying and understanding the origin of the main features observed in the various RCF layers. In Figs. 4(a)–4(c), the optical density distribution expected in the corresponding RCF layers of Fig. 3 after propagation of the proton beam in the field of a discharging microsphere. Distances and dimensions are as in the experiment. The simulation uses the experimental proton spectrum and takes into account the response of each active layer to protons of different energy. Figure 4(d) shows the charge evolution inferred from the experimental data (points) on the basis of electrostatic considerations, and the dynamic function used in the simulation (line). The simulations are important in interpreting the various features observed in the data. Indeed, associating a single proton energy E_p and, consequently, a time delay t_0 to a certain layer is valid only as a first approximation. In reality, protons with energy higher than E_p will also contribute to some extent to the dose released in the layer. Therefore, the layer will also contain information relating to the field distribution at times earlier than t_0. By reconstructing layer by layer the optical density patterns and comparing them with the experimental data, the code PTRACE permits obtaining more detailed information on the target charge history. The curve plotted in Fig. 4(d) (a Lorentzian before the peak, a decreasing exponential after the peak) was chosen as it was the one that best reproduced the general characteristics of the data (e.g., diameter and thickness of the rings).

A simple explanation of the phenomenon observed is as follows: During the interaction, as soon as the intensity is sufficiently high, a population of suprathermal electrons is generated in the interaction region.[28] Their energy distribution can be described by a Boltzmann exponential, with temperature depending on the instantaneous laser intensity. Due to their kinetic energy, the fast electrons tend to escape from the target. As the electrons escape, the target remains positively charged. The subsequent fast electron motion is, therefore, affected by the Coulomb potential of the target. While a fraction of the electrons has enough energy to escape from this potential, lower-energy electrons will reach a maximum distance and move back into the target. Estimates for the escaped fraction in conditions consistent with the experimental observations indicate that about 35% of the electrons can escape, while typical return times for the trapped electrons are of the order of a fraction of 1 ps. Therefore, the charge detected in the experiment must be only due to the electrons which have escaped the electrostatic potential. The measured charge $Q \sim 10^{-8}$ C corresponds to $\sim 10^{11}$ electrons leaving the target. If one takes 1 MeV as an indicative energy for the escaping electrons, they would carry about 1% of the laser energy. These numbers are consistent with reported experimental measurements.[29]

The charge of the target grows as long as the instantaneous laser intensity is increased, since electrons with higher energies are produced and are able to leave the target. The discharge observed following the peak of the interaction pulse is most likely due to charge redistribution in the target and stalk supporting it. To our knowledge, it is the first time that charge neutralization via redistribution of charge is observed on these timescales, and this provides an example of the fundamental physical processes that can now be investigated using the proton imaging diagnostic.

V. DETECTION OF FILAMENTARY FIELDS ASSOCIATED TO ELECTROMAGNETIC INSTABILITIES

During the discharge following the peak of the interaction pulse, the onset of filamentary structures in the proton beam pattern is observed. This is evident in Figs. 2(d), 3(c), and 3(d), where striations normal to the target surface are seen to extend for several hundred microns. It is reasonable to assume that such structures correspond to filamentary field patterns arising in the proximity of the target immediately after the peak of the pulse. Several mechanisms could be responsible for such a field configuration. As discussed in Sec. IV, a fraction of the hot electrons produced at the peak of the interaction pulse escapes from the potential of the target, but most of the electrons are dragged back into the target. This creates a current configuration which is highly unstable, as the hot electrons flowing back into the target must draw back from the target a neutralizing cold electron current. It is well known that in presence of two counterstreaming electron currents Weibel-type electromagnetic instabilities can favorably grow.[30] The electrothermal instability,[31] which takes place in presence of counterstreaming flows of collisionless hot electrons and cold collisional electrons, is particularly relevant to our experimental conditions. The growth of such an instability can lead to magnetized current filamentation at the target surface. Subsequent plasma expansion can drive the filaments outward, normal to the target surface. Each structure will be surrounded by a magnetic field, azimuthal with respect to the axis of the filament. A radial electric field, balancing the electron pressure, will also be present inside the filament. The effect of these fields on the proton probe can generate the filamentary pattern observed in the proton images taken after the interaction.

This assumption has been tested using the particle-tracing code, by adding filamentary field structures to the field configuration used in the simulation of Fig. 4. Filaments with a 5 μm radius and 15 μm spacing have been assumed, and the effect of azimuthal magnetic fields and of radial electric fields has been considered separately. It has been found that, if an appropriate magnitude is chosen, both field configurations can produce patterns as observed in the experimental data.

The diagnostic has also been applied to the detection of the fields generated following ultraintense laser propagation through underdense plasmas. The measurements, not reported here for lack of space, have revealed the existence of ''bubblelike'' structures,[32] which have been associated with structures known as postsolitons predicted by particle-in-cell simulations.[33]

VI. CONCLUSION

The examples given in Sec. V confirm that proton imaging, possibly coupled to computational analysis and modeling tools, is a powerful diagnostic for field detection in laser–plasma experiments. In particular, by using this diagnostic, the measurement of very large highly transient electric fields in plasmas has been obtained, determining their evolution on a picosecond scale with micron spatial resolution.

ACKNOWLEDGMENTS

The authors acknowledge the help of the Rutherford Appleton Laboratory staff with the experiment, and the contribution to the project of H. Ruhl (GA, San Diego, CA). The work was funded by ESPRC grants.

[1] P. Mora, Plasma Phys. Controlled Fusion **43**, A31 (2001).
[2] D. Umstadter, Phys. Plasmas **8**, 1774 (2001).
[3] F. Brunel, Phys. Rev. Lett. **59**, 52 (1987).
[4] T. M. Antonsen Jr. and P. Mora, Phys. Rev. Lett. **69**, 2204 (1992).
[5] S. C. Wilks, Phys. Fluids B **5**, 2603 (1993).
[6] A. Pukhov, Z. M. Sheng, and J. Meyer-ter-Vehn, Phys. Plasmas **6**, 2847 (1999).
[7] A. Pukhov and J. Meyer-ter-Vehn, Phys. Rev. Lett. **79**, 2686 (1997).
[8] J. R. Davies, A. R. Bell, and M. Tatarakis, Phys. Rev. E **59**, 6032 (1999).
[9] S. C. Wilks, A. B. Langdon, T. E. Cowan, M. Roth, M. Singh, S. Hatchett, M. H. Key, D. Pennington, A. Mackinnon, and R. A. Snavely, Phys. Plasmas **8**, 542 (2001).
[10] M. Tabak, J. Hammer, M. Glinsky, W. L. Kruer, S. C. Wilks, J. Woodworth, E. M. Cambell, M. D. Perry, and R. Mason, Phys. Plasmas **1**, 1626 (1994).
[11] F. Pisani, A. Bernardinello, D. Batani, A. Antonicci, E. Martinolli, M. Koenig, L. Gremillet, F. Amiranoff, S. Baton, J. Davies, T. Hall, D. Scott, P. Norreys, A. Djaoui, C. Rousseaux, P. Fews, H. Bandulet, and H. Pepin, Phys. Rev. E **62**, R5297 (2000).

[12] A. Pukhov and J. Meyer-ter-Vehn, Phys. Rev. Lett. **79**, 2686 (1997).
[13] F. Califano, N. Attico, F. Pegoraro, G. Bertin, and S. V. Bulanov, Phys. Rev. Lett. **86**, 5293 (2001).
[14] M. Honda, J. Meyer-ter-Vehn, and Pukhov, Phys. Plasmas **7**, 1302 (2000).
[15] J. A. Stamper and B. H. Ripin, Phys. Rev. Lett. **34**, 138 (1975); M. Borghesi, A. J. MacKinnon, A. R. Bell, R. Gaillard, and O. Willi, *ibid.* **81**, 112 (1998).
[16] M. Tatarakis, I. Watts, F. N. Beg, E. L. Clark, A. E. Dangor, A. Gopal, M. G. Haines, P. A. Norreys, U. Wagner, M.-S. Wei, M. Zepf, and K. Krushelnick, Nature (London) **415**, 280 (2002).
[17] C. W. Mendel Jr. and J. N. Olsen, Phys. Rev. Lett. **34**, 859 (1975).
[18] M. Markovits and A. E. Blaugrund, Phys. Fluids **30**, 1853 (1987).
[19] E. L. Clark, K. Krushelnick, J. R. Davies, M. Zepf, M. Tatarakis, F. N. Beg, A. Machacek, P. A. Norreys, M. I. K. Santala, I. Watts, and A. E. Dangor, Phys. Rev. Lett. **84**, 670 (2000); R. A. Snavely, M. H. Key, S. P. Hatchett, T. E. Cowan, M. Roth, T. W. Phillips, M. A. Stoyer, E. A. Henry, T. C. Sangster, M. S. Singh, S. C. Wilks, A. MacKinnon, A. Offenberger, D. M. Pennington, K. Yasuike, A. B. Langdon, B. F. Lasinski, J. Johnson, M. D. Perry, and E. M. Campbell, *ibid.* **85**, 2945 (2000); A. Maksimchuk, S. Gu, K. Flippo, D. Umstadter, and V. Yu. Bychenkov, *ibid.* **84**, 4108 (2000); A. J. Mackinnon, M. Borghesi, S. Hatchett, M. H. Key, P. Patel, D. H. Campbell, A. Schiavi, R. Snavely, and O. Willi, *ibid.* **86**, 1769 (2001).
[20] S. J. Gitomer, R. D. Jones, F. Begay, A. W. Ehler, J. F. Kephart, and R. Kristal, Phys. Fluids **29**, 2679 (1984); A. P. Fews, P. A. Norreys, F. N. Beg, A. R. Bell, A. E. Dangor, C. N. Danson, P. Lee, and S. J. Rose, Phys. Rev. Lett. **73**, 1801 (1994).
[21] A. Pukhov, Phys. Rev. Lett. **86**, 3562 (2001); H. Ruhl, S. V. Bulanov, T. E. Cowan, T. V. Liseikina, P. Nickles, F. Pegoraro, M. Roth, and W. Sandner, Plasma Phys. Rep. **27**, 363 (2001); S. V. Bulanov *et al.*, *Reviews of Plasma Physics* (Kluwer, New York, 2001), Vol. 22, p. 227.
[22] S. Wilks, A. B. Langdon, T. E. Cowan, M. Roth, M. Singh, S. Hatchett, M. H. Key, D. Pennington, A. J. Mackinnon, and R. A. Snavely, Phys. Plasmas **8**, 542 (2001).
[23] See also M. Borghesi, D. H. Campbell, A. Schiavi, M. G. Haines, O. Willi, A. J. MacKinnon, P. Patel, L. A. Gizzi, M. Galimberti, R. J. Clarke, F. Pegoraro, H. Ruhl, and S. Bulanov, Phys. Plasmas **9**, 2214 (2002); M. Borghesi, A. Schiavi, D. H. Campbell, M. G. Haines, O. Willi, A. J. MacKinnon, L. A. Gizzi, M. Galimberti, R. J. Clarke, and H. Ruhl, Plasma Phys. Controlled Fusion **43**, A267 (2001).
[24] C. Danson *et al.*, J. Mod. Opt. **45**, 1653 (1998).
[25] W. L. C. McLaughlin, J. C. Humphreys, D. Hocken, and W. J. Chappas, Nucl. Instrum. Methods Phys. Res. A **302**, 165 (1991).
[26] J. F. P. Ziegler, J. P. Biersack, and U. Littmark, *The Stopping and Range of Ions in Solids* (Pergamon, New York, 1996); www.srim.org
[27] M. Borghesi *et al.* (unpublished).
[28] F. N. Beg *et al.*, Phys. Plasmas **4**, 447 (1997).
[29] G. Malka and J. L. Miquel, Phys. Rev. Lett. **77**, 75 (1996).
[30] M. H. Key, Proceedings of the 29th Scottish Universities Summer School in Physics, St. Andrews, Scotland, August 1985, p. 29.
[31] M. G. Haines, Phys. Rev. Lett. **47**, 918 (1981).
[32] M. Borghesi, S. Bulanov, D. H. Campbell, R. J. Clarke, T. Z. Esirkepov, M. Galimberti, L. Gizzi, A. J. MacKinnon, N. Naumova, F. Pegoraro, H. Ruhl, A. Schiavi, and O. Willi, Phys. Rev. Lett. **88**, 135002 (2002).
[33] N. M. Naumova, S. V. Bulanov, T. Z. Esirkepov, D. Farina, K. Nishihara, F. Pegoraro, H. Ruhl, and A. S. Sakharov, Phys. Rev. Lett. **87**, 185004 (2001).